

Constraints on the amplitude of gravitational wave echoes from black hole ring-down using minimal assumptions

Andrea Miani,^{1,2,*} Claudia Lazzaro,^{3,4} Giovanni Andrea Prodi,^{5,2} Shubhanshu Tiwari,⁶ Marco Drago,^{7,8} Edoardo Milotti,^{9,10} and Gabriele Vedovato^{3,4}

¹*Università di Trento, Dipartimento di Fisica, I-38123 Povo, Trento, Italy*

²*INFN, Trento Institute for Fundamental Physics and Applications, I-38123 Povo, Trento, Italy*

³*Università di Padova, Dipartimento di Fisica, I-35121 Padova, Italy*

⁴*INFN, Sezione di Padova, I-35131 Padova, Italy*

⁵*Università di Trento, Dipartimento di Matematica, I-38123 Povo, Trento, Italy*

⁶*Physik-Institut, University of Zurich, Winterthurerstrasse 190, 8057 Zurich, Switzerland*

⁷*Università di Roma, Dipartimento di Fisica, I-00133 Roma, Italy*

⁸*INFN, Sezione di Roma, I-00133 Roma, Italy*

⁹*Università di Trieste, Dipartimento di Fisica, I-34127 Trieste, Italy*

¹⁰*INFN, Sezione di Trieste, I-34127 Trieste, Italy*

(Dated: February 24, 2023)

Gravitational wave echoes may appear following a compact binary coalescence if the remnant is an “exotic compact object” (ECO). ECOs are proposed alternatives to the black holes of Einstein’s general relativity theory and are predicted to possess reflective boundaries. This work reports a search for gravitational wave transients (GWTs) of generic morphology occurring shortly after ($\lesssim 1$ s) binary black hole (BBH) mergers, therefore targeting all gravitational wave echo models. We investigated the times after the ringdown for the higher signal-to-noise ratio BBHs within the public catalog GWTC-3 by the LIGO-Virgo-KAGRA collaborations (LVK). Our search is based on the coherentWaveBurst pipeline, widely used in generic searches for GWTs by the LVK, and deploys new methods to enhance its detection performances at low signal-to-noise ratios. We employ Monte Carlo simulations for estimating the detection efficiency of the search and determining the statistical significance of candidates. We find no evidence of previously undetected GWTs and our loudest candidates are morphologically consistent with known instrumental noise disturbances. Finally, we set upper limits on the amplitude of GW echoes for single BBH mergers.

I. INTRODUCTION

At the time of writing, the LIGO [1] and Virgo [2] observatories have successfully detected about 90 gravitational wave transients (GWTs) [3–5], all associated to compact binary coalescences (CBCs). More than 90% of these GWTs are identified as generated by the merger of binary black hole (BBH) systems. Recently, this worldwide observatory has expanded to include the KAGRA detector [6], and it is preparing for its upcoming fourth observing run (O4). Investigating the black hole (BH) nature through GW astronomy is therefore a very hot topic in fundamental physics, especially in view of the so-called BH information paradox [7]. The LIGO-Virgo-KAGRA collaboration (LVK) already published several results of tests of the general relativity theory (GR) [8–12], exploiting the GWTs emitted by BBHs.

Several recent papers [13–24] addressed the topic of *exotic compact objects* (ECO) [25]: possible compact objects (COs) alternative to the BHs predicted by Albert Einstein’s GR theory. Examples of ECOs include wormholes [26], boson stars [27], gravastar [28], and fuzzballs [29]. These ECO models are characterized by different astrophysical properties, like their constituent “matter”,

but they all share one physical characteristic: Planck-scale modifications of the BH event horizon due to quantum effects [17] or the presence of a surface of different nature [16, 30]. This feature would enable the emission of repeated GWTs occurring shortly after the BBH merger time, *echoes* of the ECO remnant ringdown [13, 14, 31].

In this work, we report a systematic search for echo signals of generic morphology occurring after the merger-ringdown phase of BBH GWTs [32]. The detection performance of the method is demonstrated down to low signal-to-noise (SNR) ratios, and the results are practically independent of the echo signal morphology. We also provide upper limits on the strain amplitude at earth of echoes for the loudest BBH GWTs in the LVK catalogs [3–5]. The search is based on the coherent Wave Burst pipeline (cWB) [33–37] widely used to search for generic short duration GWTs by LVK [38–40].

Section II provides a brief review of GW echo models and discusses the main characteristics of the predicted echo signals. In section III we summarize the data analysis method focusing on novel features: in particular, on the search for weak post-merger-ringdown GWTs, the simulations with software signal injections and the construction of the confidence belt on echoes’ h_{rss} [41] strain amplitude. Section IV reports the search results including detection performances, checks of robustness to different echo morphologies, and upper limits on the echoes’ h_{rss} . A comparative discussion with respect to two, pre-

* Correspondence email address: andrea.miani@unitn.it

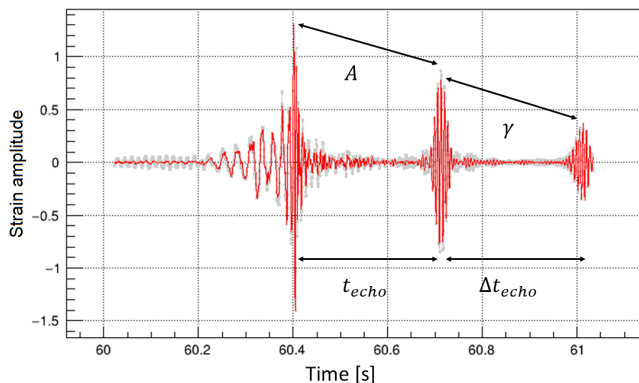


FIG. 1: Simulated inspiral-merger-ringdown-echoes (IMRE) GW transient signal vs. time at one detector: the red line is the whitened reconstructed signal strain $h(t)$; the grey line is the whitened data. The CBC signal peaks at the merger time (60.42s) and is followed by echoes, whose main parameters are visualized.

viously published, echo searches [20, 23] is reported in section V. Conclusions are drawn in section VI.

II. GRAVITATIONAL WAVE ECHOES

An ECO remnant would be characterized by an *inner barrier* located at distance r_{in} from the object's center [15, 16, 42], so

$$r_{\text{in}} = r_{\text{eh}} + l. \quad (1)$$

Here, in eq.(1), r_{eh} is the radius of the event horizon, while l is the *length correction* to the would-be BH event horizon. This length correction is theorised to be extremely small [14, 16, 17], of the order of the Planck length ($l_{\text{Planck}} \sim 2 \cdot 10^{-35}$ m). The inner barrier, together with the *outer barrier*, i.e., the effective potential barrier of the ECO, forms a cavity that traps the inbound GW radiation emitted by the CBC merger and ringdown. At each round-trip, a fraction of the trapped GW transient is radiated away, generating a train of GW pulses, called *echoes* [43].

Here we assume for simplicity a non-rotating ECO remnant, as done by many echo searches in the literature [17–23], since it is good enough for our method. A complete description of a possible echo template for a spinning ECO remnant, as expected from a compact binary coalescence, is provided in [14].

The main parameters characterizing the models of echoes are [20, 21] (see also figure 1):

- Δt_{echo} : the time separation between subsequent pulses as measured by a distant observer. It corresponds to the round-trip travel time of the GW transient between the inner and outer barriers [16];
- t_{echo} : the delay of the first echo pulse from the coalescence time of the binary. In general $t_{\text{echo}} \sim$

Δt_{echo} apart from small effects related to the strong non-linearity close to the merger time;

- γ : the attenuation per round-trip in terms of the GW amplitude ratio between subsequent echo pulses ($0 < \gamma < 1$);
- A : amplitude ratio between the first echo amplitude and the amplitude at merger time ($0 \leq A < 1$).

Following [15, 16], the theoretical prediction for Δt_{echo} is clearly related to the space-time geometry outside the ECO remnant:

$$\Delta t_{\text{echo}} \sim 2 \int_{r_{\text{in}}}^{r_{\text{out}}} \frac{1}{\sqrt{F(r)B(r)}} dr \quad (2)$$

where in eq. 2, $F(r)$ and $1/B(r)$ ¹ are the coefficients functions for the time and radial component of the metric in a spherically symmetric system, r_{in} is the radius of the inner barrier and r_{out} the radius of the outer barrier.

Eq. 2 takes into account the effects of the redshift and the spatial curvature on the GW echo scattering process. The resulting approximate expression for the time separation is [15, 16]:

$$\Delta t_{\text{echo}} \approx 54 \left(\frac{n}{4} \right) M_{30} \left[1 - 0.001 \ln \left(\frac{l/l_{\text{Planck}}}{M_{30}} \right) \right] \text{ ms}. \quad (3)$$

Here, n is a parameter of the order of the unity that takes into account the structure of the ECO nature [16, 19], $M_{30} \equiv M/30M_{\odot}$ with M standing for the final mass of the remnant. Therefore, a measurement of Δt_{echo} would provide information over the theorized nature of the ECO through the parameters n and l , related to the compactness of the ECO [13]. According to eq.(3), typical values for echoes time separation are $\Delta t_{\text{echo}} \in (30, 400)$ ms for BBH mergers whose total mass ranges in $\in (10, 100) M_{\odot}$, like most of those detected during O1, O2 and O3 by the LV Collaborations [3–5].

A. Signal proxy for echoes

The generic template we use to mimic echo signals $h_{\text{echo}}(t)$ is a double sine-Gaussian (SGE) pulse $h_{\text{echo}}(t) = h_{\text{SGE}}(t) + \gamma \cdot h_{\text{SGE}}(t + \Delta t_{\text{echo}})$ with $h_{\text{SGE}}(t)$ [44]:

$$h_{\text{SGE}}(t) = h_0 e^{-\frac{(t-t_0)^2}{\tau^2}} \cos(2\pi f_0 t + \phi_0). \quad (4)$$

¹ The space-time geometry outside an ECO remnant can be described with the $ds^2 = -F(r)dt^2 + 1/B(r)dr^2 + r^2 d\Omega^2$ metric. Such a metric is used to generally describe a CO with spherical symmetry and matter localised only in the region $r < r_{\text{shell}}$. Following Birkhoff's theorem, in the region $r > r_{\text{shell}}$ the Schwarzschild metric holds: $F(r) = B(r) = \left(1 - \frac{2GM}{c^2 r}\right)$.

In eq.(4), h_0 is the signal amplitude, t_0 the central time of the SGE, τ the half-time duration of the pulse, f_0 and ϕ_0 its central frequency and phase respectively. The values we select for these parameters are:

- h_0 is defined as $h_0 = A \cdot h_{\max}$, where h_{\max} is the GW amplitude at the merger. In our simulations, A is randomly selected per each injection within a uniform distribution $0 < A < 1$ (see III C).
- $\gamma = 0.5$ so that the second echo is contributing 1/3 of the injected SNR. This is an intermediate condition on the concentration of the signal in time and makes possible to study the reconstruction of a weaker echo, separately from the first.
- $\tau = 20$ ms and $f_0 = 140$ Hz, are close to expectations for the typical mass range of BBH mergers in GWTC-3.
- $\phi_0 = 0$. This is not impacting the results since the search method is agnostic on the signal phase in each pulse.
- $t_{\text{echo}} = 300$ ms and $\Delta t_{\text{echo}} = 300$ ms are intermediate values for the investigated BBH mergers (see section IV A) according to eq. 3.

Furthermore, the sky location of the echo signal proxy is the same as the BBH GWT.

III. SEARCH METHODS

This section describes the methods developed to search for generic GWTs after BBH mergers, such as echo signals. The analysis is based on cWB methods and comprises Monte Carlo simulations to tune the search and interpret the results in terms of gravitational wave echoes. We call this new analysis *cWB echo signal (ES) search*.

A. Coherent WaveBurst

Coherent WaveBurst [36, 37] is a data analysis pipeline searching for generic GWT signals in the data from the LVK GW detectors network [45–47]. Designed to operate without a specific waveform model, cWB first identifies coincident excess power in the multi-resolution time-frequency (TF) representations of the detectors' strain data [35]. Then, for the selected events, cWB reconstructs the source sky location and the signal waveform of each GW candidate by means of a constrained maximum likelihood method [34].

To be robust against the non-stationary detector noise cWB employs signal-independent vetoes, reducing the initial high rate of the excess power triggers. The primary selection cut is on the network correlation coefficient c_c [33], defined as:

$$c_c = \frac{E_c}{E_c + E_{\text{null}}}, \quad (5)$$

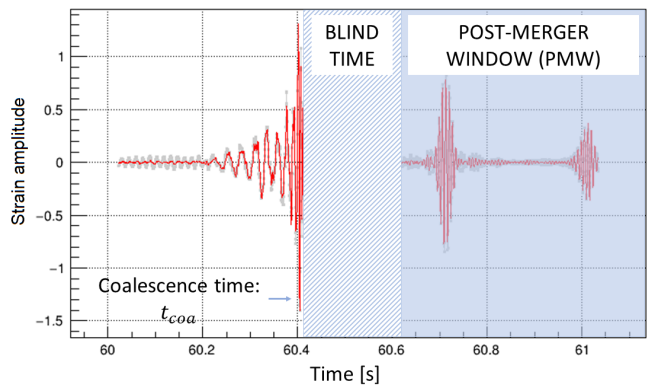


FIG. 2: This plot shows the segmentation of the analyzed time following up an event (red line). The pale blue opaque area is representative of the blind time Δt_{blind} , and the light blue transparent area after it highlights the post-merger window (PMW).

which is informative on the coherence of a signal among the detectors of the network. Here, E_c and E_{null} [33, 34, 48] are the coherent and the null energy of the signal. The algorithm also combines all the data streams into one coherent statistic η_c [33], which is used for ranking the detected events and is defined as:

$$\eta_c = \sqrt{\frac{c_c \cdot E_c}{N - 1}}, \quad (6)$$

with N the number of detectors in the network.

Typically, for a GW signal $c_c \sim 1$ while for instrumental glitches $c_c \ll 1$. By setting a threshold value on c_c , it is possible to reconstruct events with a lower or higher probability of being genuine GW signals.

In the LVK analyses, different cWB searches are used depending on the target GWT. In a previous work, cWB was used to investigate post-merger GW emission in a configuration more sensitive to the chirping morphology of the CBCs signals [49]. Currently, the most general cWB search is the all-sky burst search [38–40], with a proven ability to detect the broadest variety of GW signal morphologies. Our search method is based on this cWB instance, the same version used in the LVK O3 analysis [36, 40], thus it is more agnostic than [49], and its sensitivity is improved for post-ringdown signals with respect to all the other cWB searches.

B. Searching for echoes

Due to the expected nature of echoes, the cWB all-sky burst search is modified to select more pixels with a low energy content and scattered over a wider than usual time span (see appendix A). Triggering and final thresholds are decreased, and to group different pulses (i.e. the BBH merger and the echo-like signals) into a single event, we increase the maximum time separation

between disjoint clusters of pixels which define a single event. Specifically, the η_c threshold is decreased from 5.0 to 3.5, and the T_{gap} parameter [37] is increased up to 2 s. Also, the whitening [50] of the data is performed using a different TF map resolution to decrease the leakage of the ring-down signal of the remnant into the subsequent TF pixels. Indeed, while the cWB all-sky burst search performs the whitening in the TF map with the best frequency resolution, typically $\Delta f = 1$ Hz and $\Delta t = 0.5$ s, here we adopt a better time resolution, using pixels with a time width of $\Delta t = 0.125$ s and $\Delta f = 4$ Hz.

The search uses the BBH GWT as trigger and focuses on a user-defined post-merger time interval, called *post-merger window* (PMW), see figure 2. The PMW starts at time $t_{\text{start}}^{\text{PMW}}$, defined as

$$t_{\text{start}}^{\text{PMW}} = t_{\text{coa}} + \Delta t_{\text{blind}}, \quad (7)$$

where t_{coa} is the coalescence time of the BBH system and Δt_{blind} a user-defined blind time. The blind time's purpose is to mask the ring-down of the BBH signal, and its choice will be discussed later, in IIID. Limiting the ES search to a PMW allows the reduction of the noise contribution in estimating the energy content of the post-merger phase of the BBH system without penalising the capability to detect possible echo signals. We set the PMW time duration, Δt^{PMW} , equal to 1 s. Such time width is enough to include the first ~ 2 -4 echo pulses, when the ECO remnant mass is compatible with the average remnant mass of the detected BBH systems ($\sim (50, 70) M_{\odot}$) by the LVK collaboration [51], according to eq.(3).

Within the PMW, the main statistical parameters we compute are the network correlation coefficient, c_c^{PMW} , analogous to c_c (see eq.(5)), and the network signal to noise ratio of the data, SNR^{PMW} , defined as

$$\text{SNR}^{\text{PMW}} = \sqrt{\sum_k^N \sum_{j \in J} (x_{\text{rec}}[j])^2}, \quad (8)$$

where J is the set of the data pixels corresponding to the times inside Δt^{PMW} , and $x_{\text{rec}}[j]$ is the whitened reconstructed data.

While cWB can work with arbitrary detectors networks, the ES search deployed here is run only over the two LIGO detectors network (L, Livingston [1], and H, Hanford [1]), which picks up most of the GWTs' SNR.

C. Monte Carlo estimators

The ES search follows a two-track scheme: the background (BGK) analysis, and the signal (SIG) analysis. Both analyses are off-source experiments, meaning that the data do not include the times corresponding to the detected GW signals. The ES search is separately performed for each BBH GWT considered.

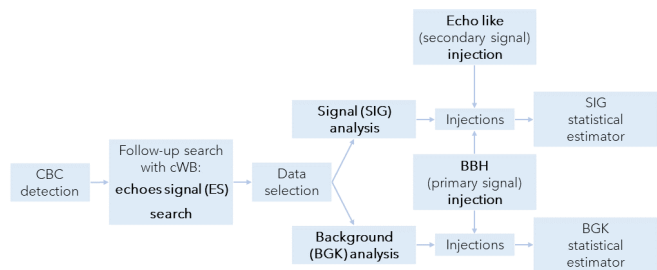


FIG. 3: Flowchart of the echo signal (ES) search. Once the cWB all-sky burst search detects a BBH event, the cWB ES search can be run as a follow-up. The search runs two parallel studies on a common data selection: the background (BGK) and the signal (SIG), and computes all the statistical estimators described in section III B. The BBH primary signal injections are randomly picked from the PE samples distribution for that event.

The **background (BGK) analysis** is used to estimate the noise statistics for the null hypothesis in the PMW. We create a set of off-source software signal injections over the data stream using waveform templates of the specific BBH event under study. These templates are randomly selected from the CBC waveform posterior samples [51], provided by the Parameter Estimation (PE) methods for the considered GW event. The signals are injected widely separated, i.e. one each 600 s, to avoid systematic effects in the analysis. This simulation is representative of the null hypothesis since by construction we inject only a BBH coalescence and no post-ringdown signals are present.

The **signal (SIG) analysis** enables the measurement of the sensitivity of the ES search to signals within the PMW. The injected BBH GWTs are the same as the BGK analysis with, in addition, the injection of *secondary signals* after each BBH merger according to the echo model of section II A. Different morphologies of secondary signals have been tested as well.

This double simulation scheme is depicted in figure 3. The data used for all studies are real data available at the GW open science centre of the LVK collaboration, see [51].

These two analyses allow us to study the detection probability, DP, and the false alarm probability, FAP, as functions of the reconstructed $\text{SNR}_{\text{rec}}^{\text{PMW}}$. Their definition is the following:

$$\text{DP} = \frac{\text{EV}_{\text{SIG}}(\text{SNR}_{\text{rec}}^{\text{PMW}} \geq th_{\text{snr}})}{\text{EV}} \quad (9)$$

$$\text{FAP} = \frac{\text{EV}_{\text{BGK}}(\text{SNR}_{\text{rec}}^{\text{PMW}} \geq th_{\text{snr}})}{\text{EV}},$$

and here EV_{SIG} and EV_{BGK} are the number of detected events above threshold in the PMW from the SIG and BGK distributions, EV is the total number of injected signals, and th_{snr} is the threshold value on SNR^{PMW} .

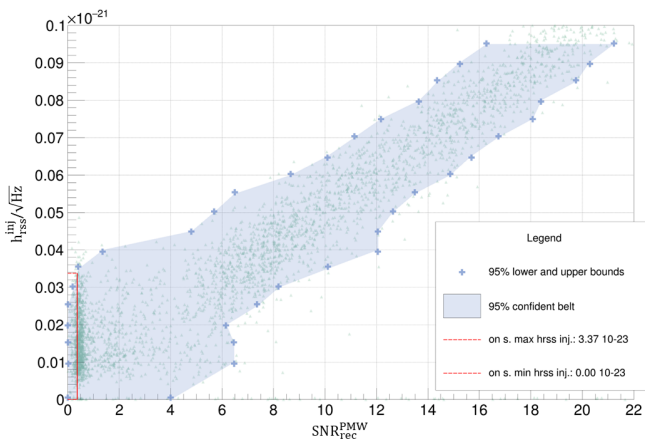


FIG. 4: Confidence belt for the echo’s injected amplitude $h_{\text{rss}}, h_{\text{rss}}^{\text{inj}}$, vs the reconstructed $\text{SNR}_{\text{rec}}^{\text{PMW}}$ in the PMW for GW150914. The blue region corresponds to 95% coverage. The on-source 95% confidence interval in terms of the h_{rss} is set by the intersection between the vertical line at the on-source value $\text{SNR}_{\text{ON}}^{\text{PMW}} \sim 0.37$ (red line) and the blue region. The y-axis values are in units of $10^{-21}/\sqrt{\text{Hz}}$.

D. Tuning of the analysis

The purpose of this tuning is the optimisation of the ES search performance before investigating the on-source GW events results. The tuning of the ES search is done by analysing the simulations related to the GW150914 event [52–54].

Thanks to the DP and FAP measurements it is possible to build the receiver operating characteristic (ROC) curves to study the ES search performances while tuning its parameters: the cWB production thresholds as well as the unique features of this search, $\Delta t_{\text{blind}}, \Delta t^{\text{PMW}}$, and c_c^{PMW} . The chosen configuration of the analysis is the one that maximises the DP for low values of FAP, in the interval $0.5\% \leq FAP \leq 5\%$. This region corresponds to the events which possess low to medium $\text{SNR}_{\text{rec}}^{\text{PMW}}$, typically $5 \leq \text{SNR}_{\text{rec}}^{\text{PMW}} \leq 8$.

The list of tested parameters and their final values are reported in appendix A. More specifically, BKG simulations show that the statistical properties of the noise background are independent of the choice of Δt_{blind} within the range (0.04, 0.4) s. Therefore, any Δt_{blind} in this range can be freely selected for the cWB ES search. Instead, the noise level starts to increase as Δt_{blind} gets shorter due to some residual leakage from the primary BBH GWT signal into the PMW. The duration of the PMW window, Δt^{PMW} , affects as expected the mean $\text{SNR}_{\text{rec}}^{\text{PMW}}$ from the BKG analysis, the longer Δt^{PMW} the larger the noise in the PMW. We selected a $\Delta t^{\text{PMW}} = 1\text{ s}$ in order to collect more echo pulses in the PMW.

E. Inference of confidence intervals

The cWB ES search can set confidence intervals on the h_{rss} [41]

$$h_{\text{rss}} = \sqrt{\int_{t \in \text{PMW}} (|h_{+}(t)|^2 + |h_{\times}(t)|^2) dt} \quad (10)$$

of signals consistent with the on-source data in the PMW. Studying the bivariate distribution of h_{rss} of the injected post-merger signals and the recovered $\text{SNR}_{\text{rec}}^{\text{PMW}}$ from SIG and BKG simulations, figure 4, one can build the confidence belt by measuring the distribution of $\text{SNR}_{\text{rec}}^{\text{PMW}}$ as a function of the injected $h_{\text{rss}}, h_{\text{rss}}^{\text{inj}}$, [55]. This is approximately achieved by introducing a binning in $h_{\text{rss}}^{\text{inj}}$ in order to preserve a minimum number of samples of hundreds per bin from the SIG analysis. This allows to target a confidence belt coverage of 95%. For the special case of $h_{\text{rss}}^{\text{inj}} = 0$, the background, we exploit the full statistics of the BKG simulation. This belt is then used to set the 95% confidence interval on h_{rss} as a function of the $\text{SNR}_{\text{rec}}^{\text{PMW}}$ value measured on-source, $\text{SNR}_{\text{ON}}^{\text{PMW}}$.

IV. RESULTS

Using the search tuning described in III D, we investigated a sub-set of 33 BBH events from the BBH detections from LVK collaboration [3–5]. The subset comprises all the BBH events that possess a network SNR greater than 10 in the cWB search for generic GWTs [38–40]². The selection is motivated by the reasonable expectation that the signal amplitude of echoes is such that $A \ll 1$, since no signal with an amplitude comparable to that of the merger has been observed after the ring-down phase of a BBH GW emission. The list of investigated BBH events and related main results is given in table I.

A. Robustness of cWB ES search

We tested the robustness of the cWB ES search against variations of the injected signals in SIG analyses, see section III C, for a few BBH GWT cases. By changing the delay time t_{eco} and time separation Δt_{echo} of the two pulses of the signal proxy defined in section II A, the detection probability at FAP=5% results unaffected as long as both pulses occur inside the analyzed time window, PMW. Therefore, the off-source results reported in this work can be considered valid as long as $\Delta t^{\text{PMW}} = 1\text{ s}$ and Δt_{blind} is included in the tested range (0.04, 0.4) s,

² The network SNR recovered by cWB is consistent to the one recovered by template searches for these loud BBH events

List of analysed BBH events							
Run - GW name	App.	t_{coa}	SNR_{net}	$h_{\text{rss}}^{50\%} \cdot \frac{10^{-23}}{\sqrt{\text{Hz}}}$	t_{echo} [s]	$\text{SNR}_{\text{ON}}^{\text{PMW}}$	p-value _{ON}
O1 - GW150914	1	1126259462.421	24.4	2.79 ± 0.02	227^{+12}_{-11}	0.4	0.819 ± 0.006
O1 - GW151012	1	1128678900.467	10.0	2.57 ± 0.03	127^{+39}_{-14}	≤ 0.1	0.53 ± 0.01
O1 - GW151226	1	1135136350.668	13.1	2.70 ± 0.03	73^{+23}_{-5}	≤ 0.1	0.79 ± 0.01
O2 - GW170104	1	1167559936.619	13.0	2.52 ± 0.01	176^{+18}_{-14}	≤ 0.1	0.888 ± 0.004
O2 - GW170608	1	1180922494.501	14.9	2.63 ± 0.01	63^{+12}_{-2}	0.5	0.069 ± 0.004
O2 - GW170729	1	1185389807.346	10.2	2.53 ± 0.01	287^{+53}_{-37}	2.5	0.041 ± 0.003
O2 - GW170809	1	1186302519.758	12.4	2.40 ± 0.02	203^{+19}_{-14}	≤ 0.1	0.56 ± 0.02
O2 - GW170814	1	1186741861.533	15.9	2.51 ± 0.02	191^{+12}_{-9}	0.3	0.450 ± 0.007
O2 - GW170823	1	1187529256.501	11.5	2.50 ± 0.02	236^{+36}_{-27}	≤ 0.1	0.835 ± 0.006
O3a - GW190408_181802	2	1238782700.279	14.7	1.82 ± 0.01	147^{+14}_{-10}	0.2	0.320 ± 0.007
O3a - GW190412	2	1239082262.165	18.9	1.82 ± 0.01	134^{+14}_{-14}	0.2	0.295 ± 0.007
O3a - GW190512_180714	2	1241719652.435	12.3	1.69 ± 0.02	123^{+14}_{-12}	≤ 0.1	0.54 ± 0.02
O3a - GW190513_205428	2	1241816086.800	12.3	1.83 ± 0.01	185^{+29}_{-21}	≤ 0.1	0.879 ± 0.004
O3a - GW190517_055101	2	1242107479.848	10.2	1.80 ± 0.02	213^{+33}_{-32}	≤ 0.1	0.52 ± 0.01
O3a - GW190519_153544	2	1242315362.418	12.0	1.84 ± 0.01	365^{+45}_{-50}	0.4	0.140 ± 0.004
O3a - GW190521	2	1242442967.471	14.4	1.74 ± 0.01	568^{+133}_{-81}	0.2	0.569 ± 0.006
O3a - GW190521_074359	2	1242459857.456	24.4	1.73 ± 0.01	256^{+23}_{-16}	4.4	0.760 ± 0.006
O3a - GW190602_175927	2	1243533585.093	12.1	1.98 ± 0.04	402^{+64}_{-54}	0.2	0.468 ± 0.007
O3a - GW190701_203306	2	1246048404.578	11.6	1.84 ± 0.01	326^{+41}_{-32}	6.4	0.0015 ± 0.0006
O3a - GW190706_222641	2	1246487219.361	12.3	1.82 ± 0.01	358^{+66}_{-49}	0.3	0.149 ± 0.005
O3a - GW190814	2	1249852257.009	22.2	1.82 ± 0.01	91^{+4}_{-3}	0.13	0.850 ± 0.004
O3a - GW190828_063405	2	1251009263.781	16.0	1.82 ± 0.01	197^{+26}_{-15}	0.2	0.205 ± 0.008
O3a - GW190915_235702	1	1252627040.693	13.1	1.88 ± 0.02	205^{+26}_{-22}	0.2	0.017 ± 0.004
O3a - GW190929_012149	1	1253755327.505	9.9	1.86 ± 0.02	367^{+122}_{-92}	0.1	0.147 ± 0.008
O3b - GW191109_010717	2	1257296855.783	17.3	1.85 ± 0.01	387^{+65}_{-54}	≤ 0.1	0.714 ± 0.008
O3b - GW191204_171526	2	1259514944.087	17.5	2.05 ± 0.05	68^{+6}_{-4}	0.1	0.31 ± 0.02
O3b - GW191215_223052	2	1260484270.995	11.2	1.69 ± 0.02	148^{+18}_{-15}	≤ 0.1	0.48 ± 0.02
O3b - GW191222_033537	2	1261020955.347	12.5	1.82 ± 0.01	272^{+55}_{-36}	≤ 0.1	0.771 ± 0.007
O3b - GW191230_180458	2	1261764316.898	14.4	1.77 ± 0.08	296^{+61}_{-40}	≤ 0.1	0.31 ± 0.04
O3b - GW200219_094415	2	1266140673.095	10.7	1.75 ± 0.07	224^{+42}_{-28}	≤ 0.1	0.27 ± 0.05
O3b - GW200224_222234	2	1266618172.381	20.0	1.74 ± 0.01	247^{+24}_{-17}	7.4	0.0011 ± 0.0004
O3b - GW200225_060421	2	1266645879.413	12.5	1.89 ± 0.04	115^{+13}_{-10}	5.5	0.05 ± 0.01
O3b - GW200311_115853	2	1267963151.380	17.8	1.80 ± 0.01	212^{+17}_{-14}	0.3	0.683 ± 0.006

TABLE I: The analyzed BBH GWs with $\text{SNR}_{\text{net}} \geq 10$ in the all-sky cWB search [38–40], listed in chronological order. Columns report the observing run; GW name; waveform model used in BGK and SIG simulations (1 = IMRPhenomPv2 approximant, 2 = SEBNRv4PHM approximant); GPS coalescence time t_{coa} to ms resolution from the PE waveform posterior information available through GWOSC [51]; network SNR as reconstructed by the cWB all-sky search for burst GWs; h_{rss} in PMW that ensures DP=50% at FAP=5%; predicted t_{echo} (following eq.(3) and assuming $n=8$, wormhole, and $l/l_{\text{Planck}} = 2$); on-source SNR inside the PMW, $\text{SNR}_{\text{ON}}^{\text{PMW}}$; p-value of $\text{SNR}_{\text{ON}}^{\text{PMW}}$ with statistical uncertainties.

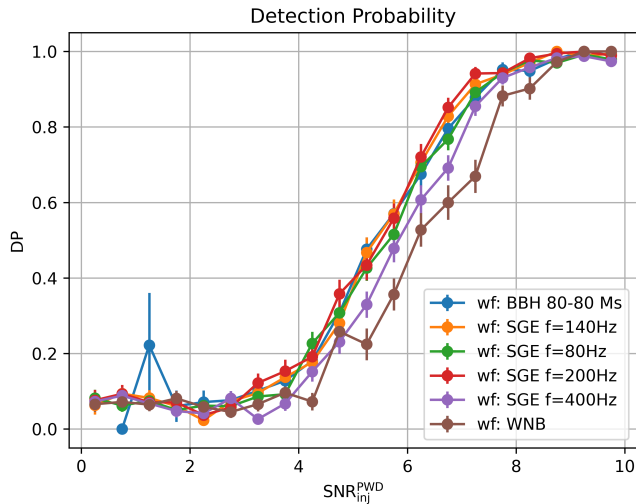


FIG. 5: Detection probability (DP) at $\text{FAP} = 5\%$ as a function of $\text{SNR}_{\text{inj}}^{\text{PMW}}$ for different morphologies of simulated post-ringdown signals: a high mass ($80 - 80M_{\odot}$) BBH coalescence (blue), trains of two elliptically polarised sine-Gaussian pulses as described in II A with different central frequencies $f_0 = 80, 140, 200, 400$ Hz (orange, green, red, and violet respectively) and a single pulse of white noise, WNB, of duration ~ 0.02 s, central frequency 150 Hz and bandwidth 100 Hz (brown). These results refer to GW150914.

regardless of the choice $t_{\text{eco}} = \Delta t_{\text{echo}} = 0.3$ s which we adopted in the SIG analyses of all BBH GWTs.

Moreover, we tested the sensitivity of the cWB ES search to widely different morphologies of post-ringdown signals, by performing additional SIG analyses. Figure 5 shows the DP at $\text{FAP} = 5\%$ as a function of the injected $\text{SNR}_{\text{inj}}^{\text{PMW}}$ for different central frequencies of the SGE echo signal proxy (see section II A), for a single pulse made by a BBH merger waveform and for a single burst of white noise. The resulting performances are almost identical within uncertainties, which is an expected outcome due to the general nature of the cWB search (see section III A). The slight decrease in performances when injecting white noise burst (WNB) signals in the PMW is mostly related to their wider frequency band.

B. Detection probability

We discuss here the detection probability measurements for the echo signal proxy described in section II A, with the requirement of $\text{FAP} = 5\%$. Figure 6 shows the DP as a function of the $h_{\text{rSS}}^{\text{inj}}$ injected inside the PMW for a subset of GWTs from the three LVK observing runs (O1, O2, O3). The visible improvement towards smaller $h_{\text{rSS}}^{\text{inj}}$ comes from the temporal enhancement of the detectors' sensitivities. Between O1 and O2 observing runs, the typical $h_{\text{rSS}}^{\text{inj}}$ at 50% DP decreases from $\sim 2.7 \cdot 10^{-23} / \sqrt{\text{Hz}}$ to $\sim 2.5 \cdot 10^{-23} / \sqrt{\text{Hz}}$. A more significant decrease in $h_{\text{rSS}}^{\text{inj}}$

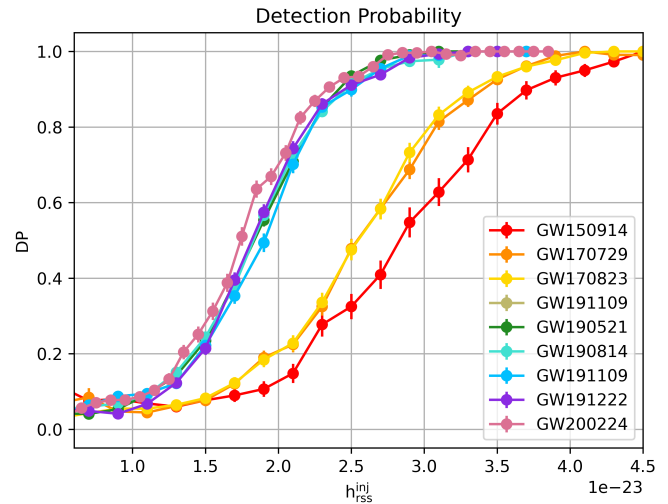


FIG. 6: Plot of the detection probability as a function of $h_{\text{rSS}}^{\text{inj}}$ of the echo signal for a selection of BBH GWTs from each observing run of the LVK. $h_{\text{rSS}}^{\text{inj}}$ units: $10^{-23} \cdot \sqrt{\text{Hz}}$. The temporal sensitivity improvement achieved is clearly visible.

at 50% DP can be seen from O2 to O3, from average values of $\sim 2.5 \cdot 10^{-23} / \sqrt{\text{Hz}}$ to $\sim 1.8 \cdot 10^{-23} / \sqrt{\text{Hz}}$, corresponding to an improvement of about 28%. Column 6 of table I reports the resulting $h_{\text{rSS}}^{\text{inj}}$ values which ensure 50% DP with $\text{FAP} 5\%$ for all the studied GWTs.

The coherent WaveBurst ES search explores a significantly lower range of $h_{\text{rSS}}^{\text{inj}}$ values with respect to the cWB all-sky search for short-duration bursts [40]. For the latter, the best results in terms of $h_{\text{rSS}}^{\text{inj}}$ values at $\text{DP}=50\%$ among the tested signal morphologies has been achieved in O3 for a single pulse SGE, $Q = 100$, $f_0 = 235$ Hz, reaching $h_{\text{rSS}}^{\text{inj}} = 8 \cdot 10^{-23} / \sqrt{\text{Hz}}$ at a FAR of one per 100 years. Here instead, with a more dispersed signal, the double pulse SGE, $Q = 8.8$, $f_0 = 140$ Hz, the average $h_{\text{rSS}}^{\text{inj}}$ values at $\text{DP}=50\%$ in O3 reaches $\sim 1.9 \cdot 10^{-23} / \sqrt{\text{Hz}}$, but at a much higher FAR of 2 per year, estimated by multiplying the FAP by the rate of the investigated BBH GWTs.

C. On-source p-value

The on-source (ON) data for each BBH GWT is analyzed using the same configuration of the cWB ES search of the SIG and BGK analyses (see sec. III C). By comparing the ON results with their BGK distributions we can estimate the p-value of $\text{SNR}_{\text{ON}}^{\text{PMW}}$ per each BBH GWT:

$$\text{p-value}_{\text{ON}} = \frac{\text{EV}_{\text{BGK}}(\text{SNR}_{\text{rec}}^{\text{PMW}} \geq \text{SNR}_{\text{ON}}^{\text{PMW}})}{\text{EV}}, \quad (11)$$

where $\text{SNR}_{\text{ON}}^{\text{PMW}}$ is the on-source reconstructed SNR inside the PMW, EV is the total number of BKG instances and EV_{BGK} is the number of BKG instances with $\text{SNR}_{\text{rec}}^{\text{PMW}}$

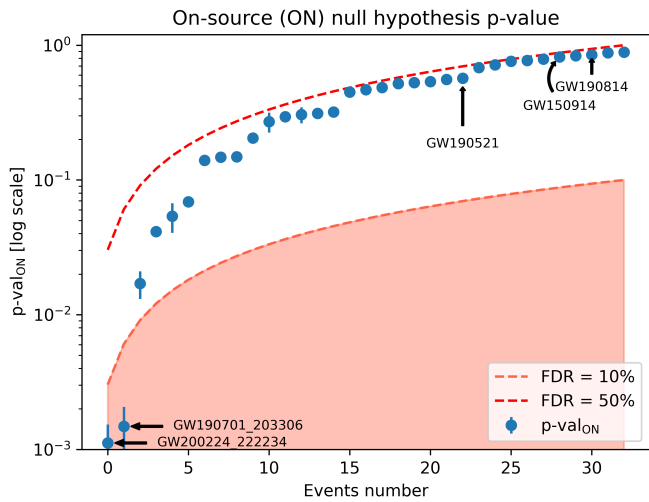


FIG. 7: Ordered p-values of $\text{SNR}_{\text{ON}}^{\text{PMW}}$ for the null hypothesis as measured by BKG analyses, blue dots with statistical uncertainties. The **red dashed line** corresponds to expected values for the null hypothesis, or to a false discovery rate $\text{FDR}=50\%$. The **orange dashed line** corresponds to $\text{FDR}=10\%$ and the **orange filled area** highlights the region in which the $\text{FDR} < 10\%$, used to select candidates.

above the ON value. A low p-value points to $\text{SNR}_{\text{ON}}^{\text{PMW}}$ on the high-energy tail of the $\text{SNR}_{\text{rec}}^{\text{PMW}}$ distribution for the null hypothesis. Columns 8 and 9 of table I list the $\text{SNR}_{\text{rec}}^{\text{ON}}$ and $\text{p-value}_{\text{ON}}$ per each BBH GWT. Figure 7 reports the p-value for each investigated GWT, ranked from the lowest to the highest. These estimates are based on the BKG analyses performed over approximately one calendar month of data around each BBH GWT. We set an a priori threshold on the false discovery rate [56], $\text{FDR} < 0.1$, to select the p-values hinting at a rejection of the null hypothesis. These cases are then the object of deeper follow-up studies.

Two GW events, GW190701 and GW200224, show an interesting $\text{SNR}_{\text{rec}}^{\text{ON}}$ and their p-values pass the a priori FDR threshold. In both cases, the morphological information of the outliers reconstructed inside the PMW (see appendix B) points to a dominant contribution by known instrumental disturbances in the frequency range (16, 40) Hz [57, 58]. These noise disturbances are known to often occur as a train of more pulses with a quasi-regular time separation. This feature is especially evident in our analysis of GW200224 (see appendix B 2) and can affect our p-values estimates, since it violates the assumption of uniformly random occurrence times and of independence of each noise pulse. Therefore, one can expect, at the very least, an underestimation of the uncertainties of our p-values.

We checked for systematic errors in the p-values of GW190701 and GW200224 by changing the off-source injection times of the BBH GWTs inside the BKG analysis. In particular, we repeated the BKG analysis using

only 4096 s of data around the GWT time. The new *local* p-value estimates are

$$\text{GW190701: } \text{p-value}_{\text{ON}}^{\text{local}} = 0.004 \pm 0.002 \quad (12)$$

$$\text{GW200224: } \text{p-value}_{\text{ON}}^{\text{local}} = 0.007 \pm 0.002, \quad (13)$$

also reported in figure 11, in appendix B. In the case of GW200224, the discrepancy between the estimates points to large systematic effects, including a significant bias of the p-value, which weakens its initial statistical significance. As for GW190701, the local p-value estimate is also higher than the initial one, though it may still be compatible within the stated statistical uncertainties.

Further statistical checks and more morphological tests on GW190701 and GW 200224 are reported in appendix B. Among these checks, the most important observation is that the reconstructed frequency spectrum for both the candidates does not match any expectation from echo models [17], so these outliers cannot be considered plausible candidates for echoes. We conclude that these two outliers are not suitable candidates for echo signals and are very likely instrumental disturbances.

For all the other GWTs, our p-value estimates occur well above our FDR threshold of attention, and their distribution is well described by the empirical BKG model. Therefore, our work does not reject the null hypothesis, confirming what was previously reported by different search methods:

- the generic echo search of [23], which estimated p-values in the post-ringdown of the GWTs detected in observing runs O1 and O2 [24] and in O3b [12];
- the template-based searches [20, 22], which provided p-value estimates for O1 GWTs plus GW170104.

We discuss the comparison of performances with the cWB ES search in section V.

D. Upper limits on h_{rSS} of echoes

The confidence belt construction procedure requires SIG analyses with extended statistics. Therefore we prioritised the GWTs detected by the cWB all-sky burst search with an $\text{SNR}_{\text{net}} \geq 15$, adding a few more GWTs close to this threshold to sample more uniformly the total mass range of the detected BBH mergers. All confidence intervals result in upper limits on the h_{rSS} of the echo signals, $h_{\text{rSS}}^{\text{UL}}$ (see table II). Typical upper limits values are in the h_{rSS} range $\sim 2 \div 3 \times 10^{-23} / \sqrt{Hz}$ at 95% coverage.

The ratios between $h_{\text{rSS}}^{\text{UL}}$ and the h_{rSS} of the primary BBH GWT, $h_{\text{rSS}}^{\text{BBH}}$ are also reported in table II. These ratios are our measured amplitude upper limits in relative terms, though their connection to the echo's A parameter (see section II) depends on the actual morphologies of echo models and of the primary BBH GWT. In the

Upper limits on echoes amplitude			
Run - GW name	SNR _{net}	$h_{\text{rss}}^{\text{UL}} \cdot \frac{10^{-23}}{\sqrt{Hz}}$	$\frac{h_{\text{rss}}^{\text{UL}}}{h_{\text{rss}}^{\text{BBH}}}$
O1 - GW150914	24.4	3.4	0.13
O2 - GW170608	14.9	3.0	0.39
O2 - GW170814	15.9	2.5	0.17
O3a - GW190408.181802	14.7	2.5	0.27
O3a - GW190412	18.9	2.2	0.20
O3a - GW190521	14.4	2.0	0.23
O3a - GW190521.074359	24.4	2.3	0.16
O3a - GW190814	22.2	2.0	0.13
O3a - GW190828.063405	16.0	2.1	0.14
O3b - GW191109.010717	17.3	2.0	0.23
O3b - GW191204.171526	17.5	2.0	0.27
O3b - GW200311.115853	17.8	2.4	0.23
O3b - GW200224.222234 [†]	20.0	~ 3.2	0.15

TABLE II: List of the BBH GWTs selected for setting confidence intervals on the echo’s amplitude. They are a subset of the loudest ones listed in table I. The columns report: GWT name; network SNR, SNR_{net}, of the GWT; upper limit in terms of h_{rss} of possible echo candidates inside the PMW, $h_{\text{rss}}^{\text{UL}}$; relative upper limit defined as the ratio between the $h_{\text{rss}}^{\text{UL}}$ and the h_{rss} of the related primary GWT, $h_{\text{rss}}^{\text{BBH}}$. †: this GWT event is affected by a loud instrumental noise in the PMW (see appendix B 2).

approximation that the merger-ringdown and each echo pulse share similar morphologies (e.g. similar central frequency and number of cycles), then the reported h_{rss} ratios can be considered to be equivalent to upper limits on A . They would be conservative upper limits in case more echo pulses are occurring within the PMW. It is clear from table II that the GWTs providing the more stringent upper limits on the relative echo amplitude are typically the louder ones, constraining the h_{rss} ratios to $\lesssim 1/8$ in case of SNR_{net} $\gtrsim 22$.

These results can be used to set observational constraints on echoes’ models, and allow projecting expected sensitivity to echoes as the detectors improve their sensitivity.

V. COMPARISON WITH PREVIOUS SEARCHES FOR ECHOES

Most of the published searches for echoes have analyzed O1 data [19–24], focusing in particular on the

GW150914 event [21, 22]. Here we provide some comments on the performances of the cWB ES search with respect to previously reported methods, being aware, however, that a full comparison of performances would require additional coordinated simulations which are computationally costly and beyond the scope of this paper. We focus on a previous model-independent search using simulated data [23], on a template-based search on GW150914 data [20], and on a very recent model-dependent analysis by [59].

Model-independent search method by Tsang et al. [23]. This general search method for echoes has been tested on two simulated data sets, assuming the two LIGO detectors at design sensitivity [60] and two noise models: pure stationary Gaussian and glitch-contaminated stationary Gaussian. The authors state that echo signals are confidently detectable above SNR = 12. This is also true for our cWB ES search, which at SNR^{PMW} = 12 preserves a 100% detection probability at a false alarm probability of 5%, on real data. Tsang, et al. also show that for echoes with SNR = 8, their false alarm probability is $\sim 6\%$ for the Gaussian noise model, while for the glitch contaminated noise increases to $\sim 30\%$. At the same SNR value and over real detector data, the cWB ES search proves a detection probability $\geq 95\%$ always at a false alarm probability of 5%. This partial comparison supports the conclusion that our cWB ES search is more competitive in the low SNR range. Moreover, our off-source simulations clearly show that the data are not compliant with a stationary Gaussian noise model in the low SNR range of interest in the proximity of most BBH GWTs.

Model-dependent search method by Westerweck et al. [20] This template-based search has been deployed on real data analyzing four BBH GWTs (including GW150914) and does not find violations of the null hypothesis. It estimates the p-values of results by using different noise instantiations close to the GWTs times, which is a similar method to our BKG analysis. Instead, the sensitivity of this search is assessed by injecting echo waveforms on simulated Gaussian noise which preserves the actual power spectral density of the LIGO detectors at the GWTs detections. Figure 2 and 5 in [20] show that peak amplitudes of echoes detach from the noise fluctuations starting from $h_p \simeq 2 \cdot 10^{-22}$. In actual noise, our search achieves 50% detection probability with a false alarm probability of 5% for a peak amplitude of the assumed echo waveform $h_p \sim 2.3 \cdot 10^{-22}$ for GW150914, as estimated from our more general result in terms of $h_{\text{rss}50\%}$ (see Tab.I). Therefore, we conclude that the sensitivity of the cWB ES search is at least competitive to that of this template-based search on this specific echo model. We remark that the implementation of the model-dependent search uses a template bank and requires subtraction of the detected GWT trigger from data prior to matched filtering for the template bank. Such steps add complexity with respect to the cWB ES search.

Model-dependent analysis by Abedi. [59] An-

other systematic search for a specific echo model has been very recently reported by Abedi [59]. This search analyses 65 GWTs from the LVK catalog of compact binary coalescences. The method assumes Gaussian noise close to each GW event. The main result reported is an upper limit value to the echo amplitude, A , resulting to be $A \leq 0.42$ with a 90% credible interval, under the assumption that A be equal for all analyzed events. In addition, the Bayes factor reported for GW190521 stands out as an outlier, suggesting a preference for post-merger echoes rather than the null hypothesis. In our study, GW190521 shows an on-source p-value equal to 0.569 ± 0.006 , suggesting that the data in the PMW are compatible with noise. Moreover, our relative upper limit on the amplitude h_{rSS} ratio at 95% coverage is 0.23 for GW190521 and is as low as 0.13 for the loudest GWTs.

VI. CONCLUSIONS

This paper describes a search for secondary gravitational wave transients of generic morphology which may occur shortly after the ringdown phase of a primary signal from a Compact Binary Coalescence. The analysis method is developed on top of the coherent WaveBurst pipeline: it uses the primary GWT as a trigger and follows up the coherent response of the interferometric gravitational wave detectors on a selectable time window, defined with respect to the merger time.

The scientific motivation for this work is the search for gravitational wave echoes after binary black hole mergers. Such echoes are expected if the final remnant object is not a standard black hole from the general relativity theory, either because the event horizon is not fully absorbing or because the remnant is an exotic compact object larger than the would-be event horizon. The detection performances of the current search are described in terms of h_{rSS} strain amplitude and are rather independent of the signal waveform and spectra within a wide signal class. Therefore, as long as any echo pulse occurs inside the selected time window, from 0.2 to 1.2 s after the merger, the reported results can be interpreted in terms of any echoes' model.

The analysis of the loudest 33 BBH mergers detected during the O1, O2 and O3 observing runs by the LIGO, Virgo and KAGRA collaborations is consistent with null results (see table I), so no evidence of echo signals is found. This search provides separate results for single BBH mergers. The off-source characterization of the detection efficiency vs false alarm probability and the estimation of p-values of candidates are performed using thousands of real detector noise instantiations. Therefore, the results do not rely on an a priori noise model and point out that the actual noise statistics is far from Gaussian in most cases, even at low SNR. The search also provides a morphological reconstruction of candidates and, for the first time, the confidence intervals on the h_{rSS} amplitude of gravitational wave echoes. The lat-

ter turn out to be upper limits, typically ranging in the interval $\sim 2 \div 3 \times 10^{-23} / \sqrt{Hz}$ in terms of h_{rSS} (see table II).

The two loudest candidates found occur after GW190701 and GW200224. These candidates are also the only ones featuring low enough p-values to require further follow-up investigations. Their morphological reconstruction clearly points to the dominating presence of known pulsating instrumental noise disturbances at low frequencies, occurring in both the LIGO detectors, and they are by far inconsistent with any published model of echoes. The pseudo-regular cadence of these disturbances is the likely cause of a systematic error in our initial p-values estimates.

To our knowledge, this search for echoes is delivering the highest and most general sensitivity to the possible presence of gravitational wave echoes. In preparation for the fourth observing run from LVK Collaboration, we plan to extend our search also to BNSs and to NS-BHs GWT signals.

Remarkably, this search can be easily modified to study other science cases of interest in current GW astronomy, because of its unmodelled nature and its adaptability. Possible examples of application fields can be the investigation of memory effects [61–65], precursors to highly eccentric BBHs [66–70], or micro-lensing effects [71, 72]. These examples share in common the predicted presence of a weak GW feature close to the coalescence time of the primary CBC GWT signal.

ACKNOWLEDGMENTS

The authors would like to thank Andrea Maselli, Francesco Salemi, and Patrick Sutton for their constructive inputs. We also acknowledge useful discussions with Sophie Bini, Alessandro Martini, and Andrea Virtuoso. This research used data, software and web tools from the Gravitational Wave Open Science Center, a service of LIGO Laboratory, the LIGO Scientific Collaboration and the Virgo Collaboration. This material is based upon work supported by NSF's LIGO Laboratory which is a major facility fully funded by the National Science Foundation. Virgo is funded by the French Centre National de Recherche Scientifique (CNRS), the Italian Istituto Nazionale di Fisica Nucleare (INFN) and the Dutch Nikhef, with contributions by Polish and Hungarian institutes. The authors are grateful for computational resources provided by the LIGO Laboratory and supported by National Science Foundation Grants PHY-0757058 and PHY-0823459. Andrea Miani thankfully acknowledges the grant provided by the EGO Consortium EGO-DIR-56-2021 and the University of Trento. Shubhan-shu Tiwari is supported by the Swiss National Science Foundation (SNSF) Ambizione Grant Number: PZ00P2-202204.

configuration parameters		
Parameters	All-Sky O3 search	ES search
bpp	0.001	0.001
subnet	0.5	0.5
c_c	0.5	0.5
η_c	5.0	3.5
A_{core}	1.7	1.7
T_{gap}	0.2 s	2.0 s
F_{gap}	128.0 Hz	128.0 Hz
SUBRHO	5.5	3.5
SUBNET	0.1	0.1
PMW	not used	$\Delta t^{\text{PMW}} = 1$ s
t_{blind}	not used	$t_{\text{blind}} \geq 40$ ms
c_c^{PMW}	not used	$c_c^{\text{PMW}} \geq 0.5$

TABLE III: Comparison of the cWB main production thresholds between all-sky burst search [40] (second column) and ES search (third column).

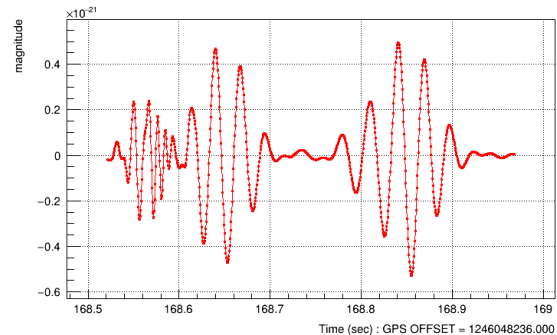
Appendix A: cWB all-sky burst search vs ES search

Table III lists cWB [36, 37] parameters (first column) and their threshold values that can be tuned in a cWB search, comparing the configuration for the cWB all-sky burst search [38–40] (second column) to that of the cWB ES search (third column). The different tuning of η_c , T_{gap} , and SUBRHO thresholds is motivated by the need to grasp lower SNR triggers in the search for echoes, while keeping under control the false alarms. Additional configuration parameters are defined in the cWB ES search: the time width of the PMW, Δt^{PMW} ; a blind time after the coalescence time, t_{blind} ; the fraction of correlated energy in the PMW, c_c^{PMW} .

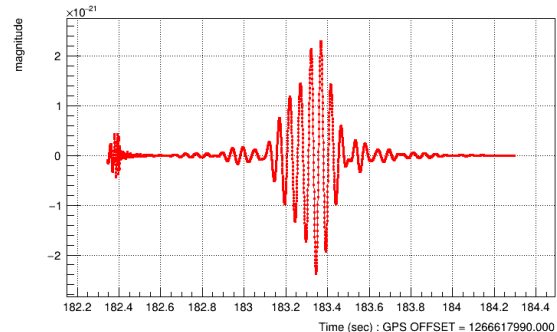
Appendix B: Followup of loudest candidates

From the analysis of the p-values of the BBH GWTs (see section IV C), two events are selected for deeper investigations since they are consistent with a FDR $\leq 10\%$: GW190701 and GW200224. Estimating the p-values on a different, more local set of noise instantiations results in higher p-values, which points to some systematic bias in our estimating procedure. Nevertheless, these two local p-values are still the only ones $\leq 1\%$, further motivating the following deeper investigations on GW190701 and GW200224.

The morphological study of the PMW on-source event allows to gather information about the reconstructed SNR of the energy excess, its arrival time, mean frequency, and the reconstructed waveform. Additional



(a) GW190701 - L1 strain.



(b) GW200224 - L1 strain.

FIG. 8: On top, Fig. 8a, is plotted the strain amplitude waveform of GW190701 and its post-merger as function of time for L1 detector. Its merger time is around ~ 168.56 s. On the bottom, Fig. 8b, reports the strain amplitude of GW200224 and its post-merger as function of time for L1 detector. Its merger time is around ~ 182.40 s. In both the scenarios are clearly visible the glitches providing the energy excesses when running the ES search.

tests have been deployed as well, like performing a single detector analysis of the on-source morphology, with the subtraction of the primary BBH waveform. The information of the morphological studies are then compared with the theoretical expectation of echo models (see section II) and with the known noise disturbances.

1. GW190701

Figure 8a, shows the reconstructed strain signal waveform of GW190701 in L1 detector. Here, the BBH signal is the smallest bump on the left while the two bumps on its right are the post-merger energy excesses. Among them, the most interesting one is the second (at time ~ 168.86 s) since it is the one falling inside our PMW. The post-merger candidate shows higher strain, and longer time duration, around ≥ 100 ms, with respect to the BBH event, and no echo models are consistent, to

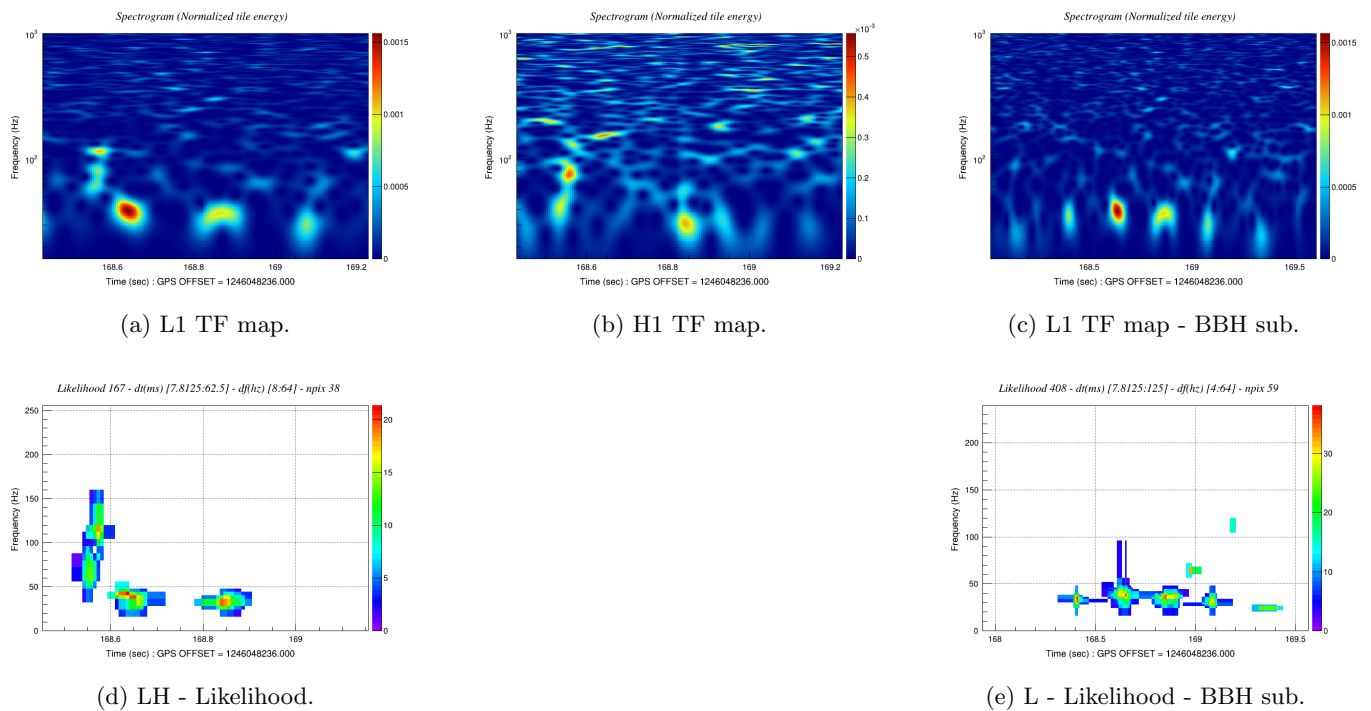


FIG. 9: In this figure: plots 9a and 9b show the time-frequency map of GW190701 event in L1 and H1 detector respectively. Plot 9c shows the event in L1 detector once the best template of GW190701 between its posterior samples is subtracted from the data. Plot 9d show the reconstructed maximum likelihood of the event for the LH network, while plot 9e display the same quantity but for a single detector search (L1) and after the best GW190701 template is subtracted from the data.

our knowledge, with these features.

The entire on-source event (BBH + PM signals) has an overall SNR content around $\text{SNR} \sim 12.9$ with a $\rho \sim 4.8$, and $c_c \sim 0.57$ that is an unusually low value for an event with such an SNR. Figures 9a and 9b, the two TF maps of the event for each detector, show that in L1-detector, after the BBH event, there are three post-merger energy excesses, at times $\sim 168.64\text{s}$, $\sim 168.86\text{s}$, and 169.97s , while in the post-merger of H1 there is only one clear energy excess at $\sim 168.84\text{s}$. This energy distribution asymmetry explains the low value of the correlation coefficient cc suggesting that a noise realisation is a preferred explanation for such an observation since it does not match up with echo signal predictions. Furthermore, in the bottom row of figure 9 there is the network on-source likelihood 9d TF map. At time $\sim 168.55\text{s}$ there is the chirping cluster of pixels representing the GW190701 event, going from frequencies around $\sim 40\text{Hz}$ up to $\sim 150\text{Hz}$, while in the post-merger, at the time $\sim 168.84\text{s}$, is clearly visible the energy excess. It has a central frequency around $f_0 \sim [30 - 40]\text{Hz}$ which is not a frequency range expected for echoes: they should possess similar frequencies or higher than the BBH merger one [17].

Finally, figure 9e shows the on-source likelihood TF map after the BBH subtraction for the single L1 detector configuration. A repetition of energy excesses either before and after GW190701 ($\sim 168.55\text{s}$) event is visi-

ble, and they have similar frequencies and morphologies, hinting at possible noisy features polluting the detector data.

2. GW200224

To study the post-merger on-source energy excess detected in GW200224 we deploy the same strategy in GW190701. Figure 8b shows the on-source strain waveform of the entire event, with the BBH being the small signal on the left. The time duration of the PM signal, $\sim 400\text{ms}$ as well as its time distance of $\sim 1\text{s}$ to the merger time of the BBH do not match the theoretical predictions of echo signals. Following eq.(3) t_{echo} is predicted to be $\sim \text{ms}$ after t_{coa} . Moreover, the TF map of the on-source event, figure 10a shows that the mean frequency of this PM excess of energy is around 40Hz well below the expected frequency values for echoes.

Figures 10a and 10b, the TF maps of the event in L1 and H1 respectively, shows that the PM signal is present only in L1 detector, while in H1 such high energy excess is not reconstructed. Since the two LIGO detectors are nearly aligned and are sensitive to the same GW's polarisation, for real astrophysical events such energy imbalance in the detectors is suspicious.

We proceed in subtracting to GW200224 on-source

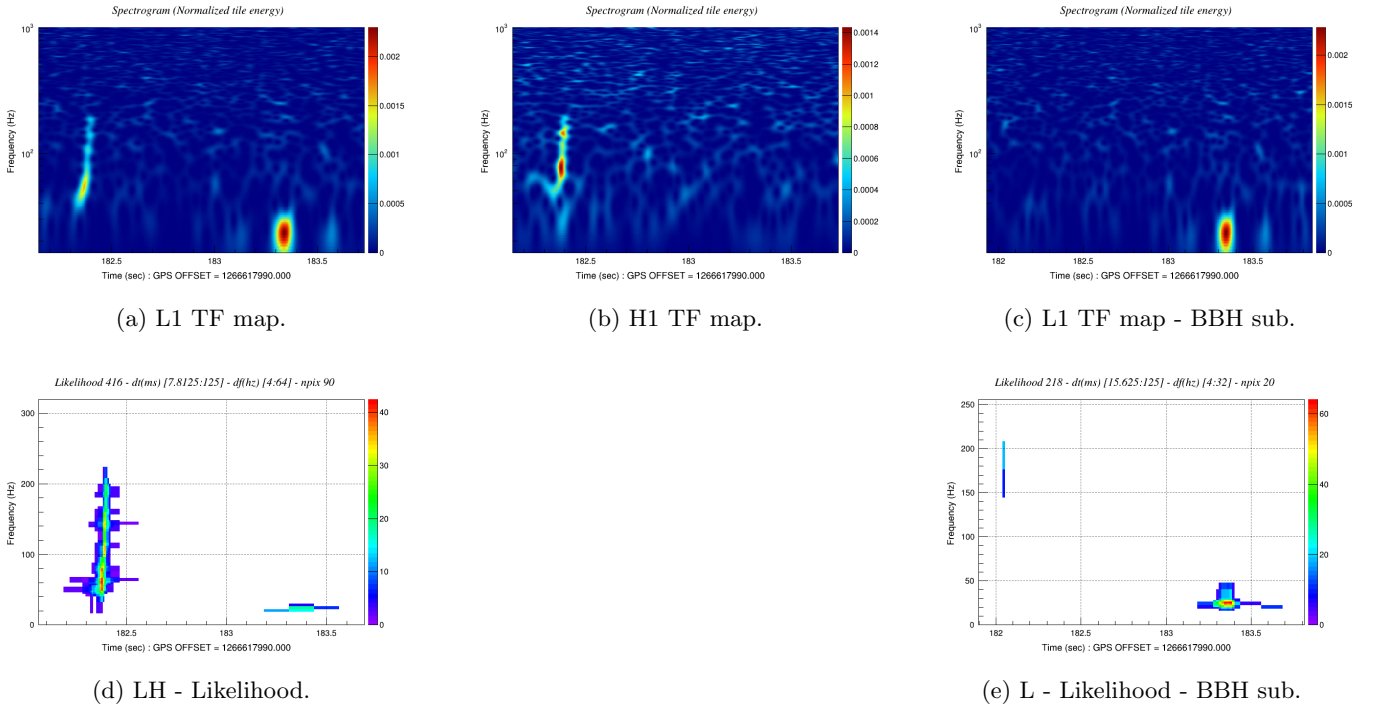


FIG. 10: In this figure: plots 10a and 10b show the time-frequency map of GW200224 event in L1 and H1 detector respectively. Plot 10c shows the event in L1 detector once the best template of GW200224 between its posterior samples is subtracted from the data. Plot 10d show the reconstructed maximum likelihood of the event for the LH network, while plot 10e display the same quantity but for a single detector search (L1) and after the best GW200224 template is subtracted from the data.

event the best PE model describing that same BBH event, then on the subtracted data we run the single detector ES search. The result is displayed in figure 10e. Here, no undetected energy excess other than the investigated one appears, suggesting that we are not in a scenario similar to the single detector analysis of GW190701. The energy outlier has a SNR ~ 10.4 , while the overall SNR of the BBH signal plus post-merger excess of energy is equal to ~ 16.8 (in single detector mode).

3. cWB ES search with 32 Hz mitigation

The PMW on-source morphologies hint to a possible data pollution by a glitch family identified in the frequency range $\in (16, 40)$ Hz [57, 58]. Therefore, we repeated the ES search for these two GWs by including a specific single detector data filter [73, 74] that estimates the power oscillations within the frequency range $\in (16 - 40)$ Hz and attenuates them. We label such analysis as 32 Hz-ES search, to differentiate it from the standard ES search. The measured on-source null hypothesis p-values when the noise around 32 Hz frequencies is mit-

igated result:

$$\text{GW190701: } p\text{-value}_{\text{ON}}^{32\text{Hz}} = 0.024 \pm 0.002 \quad (\text{B1})$$

$$\text{GW200224: } p\text{-value}_{\text{ON}}^{32\text{Hz}} = 0.003 \pm 0.001 \quad (\text{B2})$$

and they are plotted in figure 11 as the violet dots. This noise mitigation rules out the post-merger event candidate GW190701, while for the PM of GW200224 the p-value is still within the $\text{FRD} \leq 10\%$.

This study together with the morphological investigation of the PMW energy excesses of GW190701 and GW200224 (see appendix B 1 and B 2), show that it is reasonable to assume them to be non stationary noise feature polluting the data and especially affecting L detector. These noise transients possess a central frequency around (30, 40) Hz, and have a greater time duration (\sim hundred of ms) with respect to the expected one for echo signals (\sim tens of ms), so around one order of magnitude bigger.

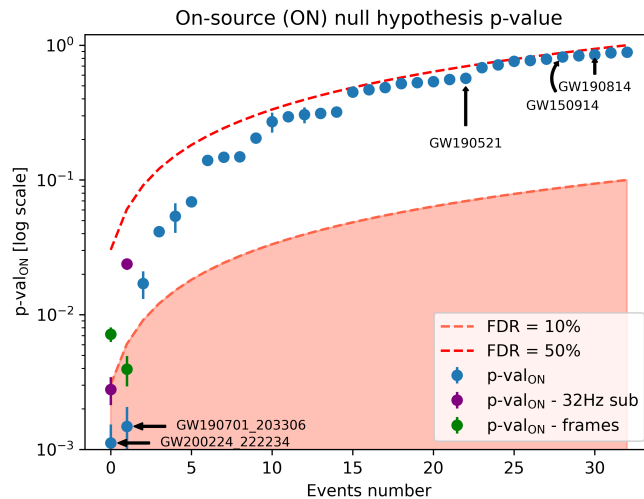


FIG. 11: Same plot of figure 7, where the **green dots** are the on-source p-value obtained from the ES search carried on using only the 4096s around the main BBH event. The **violet dots** are the on-source p-value for the ES search performed over the same standard analysis data but applying a 32 Hz data mitigation plugin to suppress some noisy contaminating the O3a and O3b observational periods.

-
- [1] The LIGO Scientific Collaboration, *Advanced LIGO, Classical and Quantum Gravity* **32**, 074001 (2015).
- [2] The Virgo Scientific Collaboration, *Advanced Virgo: a second-generation interferometric gravitational wave detector*, *Classical and Quantum Gravity* **32**, 024001 (2014).
- [3] Abbott, B. P. and others (LIGO Scientific Collaboration and Virgo Collaboration), *GWTC-1: A Gravitational-Wave Transient Catalog of Compact Binary Mergers Observed by LIGO and Virgo during the First and Second Observing Runs*, *Phys. Rev. X* **9**, 031040 (2019).
- [4] Abbott, R. and others (LIGO Scientific Collaboration and Virgo Collaboration), *GWTC-2: Compact Binary Coalescences Observed by LIGO and Virgo during the First Half of the Third Observing Run*, *Phys. Rev. X* **11**, 021053 (2021).
- [5] Abbott, R. and others (LIGO Scientific Collaboration and Virgo Collaboration and KAGRA Collaboration), *GWTC-3: Compact Binary Coalescences Observed by LIGO and Virgo During the Second Part of the Third Observing Run* (2021).
- [6] KAGRA: 2.5 generation interferometric gravitational wave detector, *Nature Astronomy* **3**, 10.1038/s41550-018-0658-y (2019).
- [7] W. G. Unruh *et al.*, *Information loss*, *Reports on Progress in Physics* **80**, 092002 (2017).
- [8] A. Einstein, *Die Grundlage der allgemeinen Relativitätstheorie*, *Annalen der Physik* **354**, 769 (1916).
- [9] B. P. Abbott *et al.* (LIGO Scientific and Virgo Collaborations), *Tests of general relativity with gw150914*, *Phys. Rev. Lett.* **116**, 221101 (2016).
- [10] Abbott, R. and others (LIGO Scientific Collaboration and Virgo Collaboration), *Tests of general relativity with the binary black hole signals from the LIGO-Virgo catalog GWTC-1*, *Phys. Rev. D* **100**, 104036 (2019).
- [11] Abbott, R. and others (LIGO Scientific Collaboration and Virgo Collaboration), *Tests of general relativity with binary black holes from the second LIGO-Virgo gravitational-wave transient catalog*, *Phys. Rev. D* **103**, 122002 (2021).
- [12] Abbott, R. and others (LIGO Scientific Collaboration and Virgo Collaboration and KAGRA Collaboration), *Tests of General Relativity with GWTC-3* (2021).
- [13] A. Testa *et al.*, *Analytical template for gravitational-wave echoes: Signal characterization and prospects of detection with current and future interferometers*, *Phys. Rev. D* **98**, 044018 (2018).
- [14] E. Maggio, *et al.*, *Analytical model for gravitational-wave echoes from spinning remnants*, *Phys. Rev. D* **100**, 064056 (2019).
- [15] V. Cardoso *et al.*, *Is the Gravitational-Wave Ringdown a Probe of the Event Horizon?*, *Phys. Rev. Lett.* **116**, 171101 (2016).
- [16] V. Cardoso *et al.*, *Gravitational-wave signatures of exotic compact objects and of quantum corrections at the horizon scale*, *Phys. Rev. D* **94**, 084031 (2016).
- [17] Q. Wang *et al.*, *Black hole echology: The observer’s manual*, *Phys. Rev. D* **97**, 124044 (2018).
- [18] Z. Mark *et al.*, *A recipe for echoes from exotic compact objects*, *Phys. Rev. D* **96**, 084002 (2017).
- [19] J. Abedi *et al.*, *Echoes from the abyss: Tentative evidence for Planck-scale structure at black hole horizons*, *Phys. Rev. D* **96**, 082004 (2017).
- [20] J. Westerweck *et al.*, *Low significance of evidence for black hole echoes in gravitational wave data*, *Phys. Rev. D* **97**, 124037 (2018).
- [21] A. B. Nielsen *et al.*, *Parameter estimation and statistical significance of echoes following black hole signals in the first Advanced LIGO observing run*, *Phys. Rev. D* **99**, 104012 (2019).
- [22] R. K. L. Lo *et al.*, *Template-based gravitational-wave echoes search using Bayesian model selection*, *Phys. Rev.*

- D **99**, 084052 (2019).
- [23] K. W. Tsang *et al.*, A morphology-independent data analysis method for detecting and characterizing gravitational wave echoes, *Phys. Rev. D* **98**, 024023 (2018).
- [24] K. W. Tsang *et al.*, A morphology-independent search for gravitational wave echoes in data from the first and second observing runs of Advanced LIGO and Advanced Virgo, *Phys. Rev. D* **101**, 064012 (2020).
- [25] V. Cardoso *et al.*, Tests for the existence of black holes through gravitational wave echoes, *Nat. Astron.* **1**, 586–591 (2017).
- [26] M. S. Morris *et al.*, Wormholes, Time Machines, and the Weak Energy Condition, *Phys. Rev. Lett.* **61**, 1446 (1988).
- [27] F. E. Schunck *et al.*, General relativistic boson stars, *Classical and Quantum Gravity* **20**, R301 (2003).
- [28] P. O. Mazur *et al.*, Gravitational vacuum condensate stars, *PNAS* **101**, 9545 (2004).
- [29] S. D. Mathur, The fuzzball proposal for black holes: an elementary review, *Progress of Physics* **57**, 793 (2005).
- [30] W. Rindler, Visual Horizons in World Models, *Monthly Notices of the Royal Astronomical Society* **116**, 662 (1956), <https://academic.oup.com/mnras/article-pdf/116/6/662/8077949/mnras116-0662.pdf>.
- [31] Q. Wang *et al.*, Echoes from quantum black holes, *Phys. Rev. D* **101**, 024031 (2020).
- [32] A. Miani, Agnostic method to detect low energetic signals nearby a gravitational wave transient from a binary black hole system (2022).
- [33] S. Klimentko *et al.*, Method for detection and reconstruction of gravitational wave transients with networks of advanced detectors, *Phys. Rev. D* **93**, 042004 (2016).
- [34] S. Klimentko *et al.*, A coherent method for detection of gravitational wave bursts, *Classical and Quantum Gravity* **25**, 114029 (2008).
- [35] S. Klimentko *et al.*, Constraint likelihood analysis for a network of gravitational wave detectors, *Phys. Rev. D* **72**, 122002 (2005).
- [36] M. Drago *et al.*, coherent WaveBurst, a pipeline for unmodeled gravitational-wave data analysis, *SoftwareX* **14**, 100678 (2021).
- [37] Coherent WaveBurst group, Coherent WaveBurst (2003).
- [38] Abbott, B. P. and others (LIGO Scientific Collaboration and Virgo Collaboration), All-sky search for short gravitational-wave bursts in the first Advanced LIGO run, *Phys. Rev. D* **95**, 042003 (2017).
- [39] Abbott, B. P. and others (LIGO Scientific Collaboration and Virgo Collaboration), All-sky search for short gravitational-wave bursts in the second Advanced LIGO and Advanced Virgo run, *Phys. Rev. D* **100**, 024017 (2019).
- [40] Abbott, R. and others (LIGO Scientific Collaboration, Virgo Collaboration, and KAGRA Collaboration), All-sky search for short gravitational-wave bursts in the third Advanced LIGO and Advanced Virgo run, *Phys. Rev. D* **104**, 122004 (2021).
- [41] P. J. Sutton, A Rule of Thumb for the Detectability of Gravitational-Wave Bursts (2013).
- [42] V. Cardoso *et al.*, Light rings as observational evidence for event horizons: Long-lived modes, ergoregions and nonlinear instabilities of ultracompact objects, *Phys. Rev. D* **90**, 044069 (2014).
- [43] V. Ferrari *et al.*, Scattering of particles by neutron stars: Time evolutions for axial perturbations, *Phys. Rev. D* **62**, 107504 (2000).
- [44] J. Abadie *et al.* (The LIGO Scientific Collaboration and The Virgo Collaboration), All-sky search for gravitational-wave bursts in the second joint LIGO-Virgo run, *Phys. Rev. D* **85**, 122007 (2012).
- [45] The LIGO Scientific Collaboration, LIGO Scientific Collaboration (1997).
- [46] The Virgo Collaboration, Virgo Scientific Collaboration (1997).
- [47] The KAGRA Collaboration, KAGRA Scientific Collaboration (2010).
- [48] S. Chatterji *et al.*, Coherent network analysis technique for discriminating gravitational-wave bursts from instrumental noise, *Phys. Rev. D* **74**, 082005 (2006).
- [49] F. Salemi *et al.*, Wider look at the gravitational-wave transients from GWTC-1 using an unmodeled reconstruction method, *Phys. Rev. D* **100**, 042003 (2019).
- [50] Coherent WaveBurst group, The Whitening (2018).
- [51] The LIGO Scientific Collaboration, the Virgo Collaboration, and the KAGRA Collaboration, Gravitational Wave Open Science Center (2018).
- [52] B. P. Abbott *et al.* (LIGO Scientific Collaboration and Virgo Collaboration), Observation of Gravitational Waves from a Binary Black Hole Merger, *Phys. Rev. Lett.* **116**, 061102 (2016).
- [53] B. P. Abbott *et al.* (LIGO Scientific Collaboration and Virgo Collaboration), Observing gravitational-wave transient GW150914 with minimal assumptions, *Phys. Rev. D* **93**, 122004 (2016).
- [54] B. P. Abbott *et al.* (LIGO Scientific Collaboration and Virgo Collaboration), Properties of the Binary Black Hole Merger GW150914, *Phys. Rev. Lett.* **116**, 241102 (2016).
- [55] N. J., Outline of a Theory of Statistical Estimation Based on the Classical Theory of Probability, *Philosophical Transactions of the Royal Society of London* **236**, 333–380 (1937).
- [56] C. J. Miller *et al.*, Controlling the False-Discovery Rate in Astrophysical Data Analysis, *The Astronomical Journal* **122**, 3492 (2001).
- [57] M. Cabero *et al.*, Blip glitches in Advanced LIGO data, *Classical and Quantum Gravity* **36**, 155010 (2019).
- [58] B. P. Abbott *et al.* (The LIGO Scientific Collaboration and The Virgo Collaboration), Effects of data quality vetoes on a search for compact binary coalescences in Advanced LIGO’s first observing run, *Classical and Quantum Gravity* **35**, 065010 (2018).
- [59] Search for echoes on the edge of quantum black holes, author = Abedi, Jahed (2022).
- [60] Abbott, B. P. and others (LIGO Scientific Collaboration and Virgo Collaboration), Prospects for Observing and Localizing Gravitational-Wave Transients with Advanced LIGO and Advanced Virgo, *Living Rev. Relativ.* **16**, 10.1007/lrr-2016-1 (2016).
- [61] D. Christodoulou, Nonlinear nature of gravitation and gravitational-wave experiments, *Phys. Rev. Lett.* **67**, 1486 (1991).
- [62] M. Favata, The gravitational-wave memory effect, *Classical and Quantum Gravity* **27**, 084036 (2010).
- [63] M. Hübner *et al.*, Measuring gravitational-wave memory in the first LIGO/Virgo gravitational-wave transient catalog, *Phys. Rev. D* **101**, 023011 (2020).
- [64] M. Hübner *et al.*, Memory remains undetected: Updates from the second LIGO/Virgo gravitational-wave tran-

- sient catalog, *Phys. Rev. D* **104**, 023004 (2021).
- [65] S. Tiwari *et al.*, Leveraging gravitational-wave memory to distinguish neutron star-black hole binaries from black hole binaries, *Phys. Rev. D* **104**, 123024 (2021), arXiv:2110.11171 [gr-qc].
- [66] Y. Setyawati *et al.*, Adding eccentricity to quasicircular binary-black-hole waveform models, *Phys. Rev. D* **103**, 124011 (2021).
- [67] M. Ebersold *et al.*, Search for nonlinear memory from subsolar mass compact binary mergers, *Phys. Rev. D* **101**, 104041 (2020).
- [68] B. P. Abbott *et al.* (LIGO Scientific Collaboration and Virgo Collaboration), Search for Eccentric Binary Black Hole Mergers with Advanced LIGO and Advanced Virgo during Their First and Second Observing Runs, *The Astrophysical Journal* **883**, 149 (2019).
- [69] R. Gamba *et al.*, GW190521 as a dynamical capture of two nonspinning black holes, *Nature Astronomy* **7**, 11 (2022).
- [70] M. Ebersold *et al.*, Observational limits on the rate of radiation-driven binary black hole capture events, *Phys. Rev. D* **106**, 104014 (2022).
- [71] J. M. Ezquiaga *et al.*, Phase effects from strong gravitational lensing of gravitational waves, *Phys. Rev. D* **103**, 064047 (2021).
- [72] R. Abbott *et al.*, Search for Lensing Signatures in the Gravitational-Wave Observations from the First Half of LIGO–Virgo’s Third Observing Run, *The Astrophysical Journal* **923**, 14 (2021).
- [73] M. Szczepańczyk *et al.*, Observing an intermediate-mass black hole GW190521 with minimal assumptions, *Phys. Rev. D* **103**, 082002 (2021).
- [74] V. Tiwari *et al.*, Regression of environmental noise in LIGO data, *Classical and Quantum Gravity* **32**, 165014 (2015).